Prediction of the Reaction Forces of Spiral-Groove Gas Journal Bearings by Artificial Neural Network Regression Models

Elia Iseli[a,*], Jürg Schiffmann[b]

[a]Fischer AG, Ernst Fischer-Weg 5, CH-3360 Herzogenbuchsee, Switzerland
[b]Ecole Polytechnique Fédérale Lausanne, EPFL STI IGM LAMD, Maladière 71b, CP526, CH-2002 Neuchâtel 2, Switzerland

ARTICLE INFO

Keywords:
Neural network regression, Meta-modelling, Compressible Reynolds equation, Aerodynamic lubrication, Herringbone Groove Journal Bearing

ABSTRACT

This paper presents neural network regression models for predicting the static and dynamic reaction forces of spiral grooved gas journal bearings. The partial differential equations (PDEs) are sampled, based on a full factorial and randomly spaced parameter set. Feed-forward neural network (FNN) architectures are developed for modeling the PDEs and therefore replacing the time-consuming discrete and iterative solution procedure used to this date. A significant speed-up factor of $> 10^3$ in computation time is achieved, compared to solving the PDE numerically. Furthermore, the FNN allows for multi-dimensional interpolation, which makes global system optimization easily possible. This is demonstrated by a real-case rotordynamic system optimization. By using the neural network meta-models, a complete rotordynamic system optimization time reduction of factor 300 is achieved.

1. Introduction

High-speed small scale turbomachinery is used in many different energy conversion systems such as domestic or commercial heat pumps [20], Organic Rankine cycles [18] or fuel cells [24]. The requirements of high rotational speeds and a high life-time expectation make gas lubricated bearings ideal for these systems. Gas bearings, such as the herringbone-groove journal bearing (HGJB), offer the advantages of oil-free operation, long lifetime, high rotational speed at relatively low frictional losses compared to other bearing types, no sealing requirements and avoidance of complex auxiliary systems. In order to develop stable compressor systems, accurate bearing models need to be available and parameter variations with thousands of computations have to be performed during an automated optimization process.

To this date, the performance of HGJB have been predicted by solving the thin-film flow equation, also called Reynolds-equation, in different ways. One of them is based on the narrow groove theory (NGT) approach, introduced by Whipple [23]. The NGT is developed by assuming an infinite number of grooves, which leads to a smooth-pressure distribution, which is governed by the NGT equation. The NGT equation intrinsically contains the bearing geometry. The NGT was further developed by Hirs [12], Malanoski and Pan [14], Vohr and Pan [21] and Vohr and Chow [22]. Fleming and Hamrock [4] used the narrow groove theory (NGT) for optimizing HGJB for maximum stability, quantified by

*Corresponding author
E-mail address: elia.iseli@fischerspindle.com (E. Iseli)
ORCID(s):

a critical mass, which represents the mass the bearing can support before it gets unstable. A more detailed numerical analysis has been published by Bonneau and Absi [1], who solved the Reynolds-equation for HGJB based on a FEM approach. They presented solutions for different number of grooves and compared the case where the grooves are rotating and non-rotating. Iseli et al. [13] introduced the finite groove approach (FGA), which allows the computation of HGJB static and dynamic reaction forces with rotating grooves, avoiding a time-consuming transient analysis. They further presented a systematic comparison between the NGT and the FGA and limitations of the NGT were presented. A detailed overview of the different modeling approaches is given by Gu et al. [6].

Nature of the issue. All of the above presented numerical methods involve time-intensive iterative procedures or lack the possibility of interpolating between different parameters. This is not a problem for the computation of one single bearing, but becomes problematic when optimization procedures require parameter variations in the order of thousands. The number of design variables for a rotordynamic system of small-scale turbo compressors is normally more than 10. For the design of such systems different analysis and optimization procedures are used, such as genetic algorithms or full factorial combinations and the number of computations easily exceeds millions. Therfore, one is interested in developing new methods, which are faster than already existing solvers.

Only a small number of prior work addresses this issue by using transfer functions of different types. Elrod et al. [3] introduced the step-jump response analysis, which was further developed by Miller and Green [15, 16]. They analyzed the reaction motion of a self-acting cylindrical bearing by imposing an initial step-jump displacement. By using the analogy between viscoelastic elements and gas films, the bearing behavior is approximated by polynomial functions. A significant speed-up was reported, however, the usage of the derived models was limited to a simplified bearing model and to one specific geometry. Hassini and Arghir [9, 10, 11] used rational transfer functions for approximating the linearized bearing parameters in the frequency domain at different eccentric shaft positions. The linearized properties were computed by solving the non-linear fluid film equation. With the inverse Laplace transformation they obtained differential equations, describing the transient gas film behavior in a linear manner. They reported a speed-up in transient computation time of factor 2 [9]. Other transfer function methods, based on series and coefficient models, have been presented by Andrés and Jeung [19] for oil-bearings and by Franssen et al. [5] for aerostatic bearings. The bearing types used by Hassini and Arghir, Andrés and Jeung and Franssen et al. show moderate non-linear behavior compared to a HGJB. In order to model a HGJB, high order rational function (more than order 4) approximations are necessary. In addition, the strong non-linear behavior of HGJB in the geometrical and operational parameter space rules out the usage of simple linear, linear with interactions and linear-quadratic with interaction regression models such as normally used in a classical design of experiment analysis. A new approach is presented in this work, which is based on artificial neural network (ANN) regression models, capable of mapping several input parameters to a highly non-linear output solution space.

Goals and objectives. The goal is the derivation of artificial neural network regression models, describing the static and dynamic HGJB behavior within a given range of varying boundary conditions to decrease the computation time in comparison to existing numerical methods.

Scope of the paper. The PDEs, describing the static and dynamic behavior of HGJB, are numerically solved at full factorial and randomly spaced data points. The solution pressure fields are integrated in space in order to obtain the bearing reaction forces. Two-layer feed-forward neural network architectures are compared and selected based on a specified regression accuracy threshold and number of total neurons used. Speed-up and accuracy comparisons between the numerical analysis and the derived neural network are discussed and the possibility of multi-dimensional interpolation is presented by means of a rotordynamic case study.

2. Problem definition

Parameters. A gas bearing is characterized by multiple geometrical design parameters as well as by operating conditions. The geometrical parameters of a HGJB are schematically shown in Fig. 1 and listed in Table 1. Seven

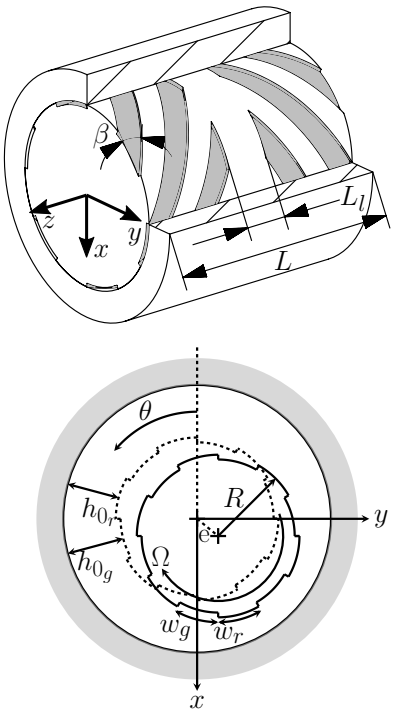

Figure 1: Spiral-grooved journal bearing convention. Upper schematic: 3D view of a HGJB. Lower schematic: cross section of HGJB. The parameters are specified in the nomenclature.

parameters in total describe a HGJB, including operational conditions, such as rotational speed and eccentricity. The

Table 1
Factors of herringbone-grooved journal bearing.

Factor	Symbol	Unit
Groove-width ratio	α	-
Groove angle	β	°
Film thickness ratio	H_{gr}	-
Length to diameter ratio	L/D	-
Land to groove ratio	γ	-
Eccentricity	ε	-
Compressibility number	Λ	-

groove-ridge ratio is specified as follows:

$$\alpha = \frac{w_g}{w_g + w_r}, \tag{1}$$

the film thickness ratio:

$$H_{gr} = \frac{h_{0g}}{h_{0r}}. \tag{2}$$

the land to groove ratio:

$$\gamma = \frac{L - L_l}{L} \tag{3}$$

and the static eccentricity:

$$\varepsilon = \frac{\mathrm{e}}{h_{0r}}. \tag{4}$$

The land to groove ratio is kept constant through the variations with a value of 1, which corresponds to a fully grooved bearing. The number of grooves is not varied, since it is assumed to be infinite based on the Narrow Groove Theory (NGT). Each parameter is given an upper and lower limit, which are listed in Table 2. The limits given in Table 2 are

Table 2
Factor ranges for regression models.

Parameter	Min	Max	Mean
α	0.3	0.7	0.5
β	10	50	30
H_{gr}	1	4	2.5
L/D	0.5	2	1.25
ε	0	0.8	0.4
Λ	0.1	40	20.5

specified based on bearing parameters presented in the literature, namely by Guenat and Schiffmann [8], who listed bearing geometries of stable HGJB-supported rotordynamic systems and Fleming and Hamrock [4], who optimized

bearings for maximum stability and published the corresponding geometrical values.

Bearing reaction forces. The reaction forces of the bearing are obtained from the fluid film pressure field, enclosed by the shaft and the bushing. The pressure inside a HGJB can be described by the NGT-equation, derived by Vohr and Chow [22]. Using the same notation for the NGT coefficients as Guenat and Schiffmann [7], the NGT equation in cylindrical coordinates for an ideal gas follows:

$$\begin{aligned}\frac{\partial}{\partial\theta}\left(P\left[f_1\frac{\partial P}{\partial\theta}+f_2\frac{\partial P}{\partial Z}+c_s f_4\sin\beta\right]\right)+\\ \frac{\partial}{\partial Z}\left(P\left[f_2\frac{\partial P}{\partial\theta}+f_3\frac{\partial P}{\partial Z}-c_s f_4\cos\beta\right]\right)=\\ 2\gamma_{ex}\Lambda\frac{\partial(Pf_5)}{\partial\tau}+\Lambda\frac{\partial(Pf_5)}{\partial\theta},\end{aligned} \tag{5}$$

where θ represents the circumferential coordinate, Z the axial coordinate, P the non-dimensional pressure, τ the non-dimensional time, β the spiral-groove angle and Λ the compressibility number (see Fig. 1 for the coordinate system convention). The compressibility number Λ is a gas bearing specific non-dimensional number and defined as follows:

$$\Lambda=\frac{6\mu R^2}{p_a h_{0r}^2}\Omega, \tag{6}$$

where μ is the gas dynamic viscosity, R the bearing radius, p_a the ambient pressure, h_{0r} the nominal bearing clearance in concentric position and Ω the rotational speed. For a given bearing geometry, the static reaction forces are only influenced by the compressibility number Λ. For fixed gas and geometrical properties, an increasing compressibility number can be understood as an increase in rotational speed. Therefore, the analysis of a gas bearing over a given speed range can be obtained in a non-dimensional way by varying the compressibility number.

The whirl ratio γ_{ex} is the ratio between the bearing excitation frequency ω_{ex} and rotational speed Ω. The coefficients f_i and c_s are specified by the bearing geometry and its operational condition. The coefficient's expressions are detailed by Guenat and Schiffmann [7].

Equation (5) represents a non-linear transient partial differential equation (PDE). In order to compute the static and dynamic HGJB properties, Eq. (5) is linearized around a given eccentricity and an excitation frequency dependent small orbital motion is imposed. This is done by introducing a perturbed clearance, varying with excitation frequency ω_{ex}:

$$H_{per}=H+\Delta x H_x(\theta)\mathrm{e}^{i\omega_{ex}t}+\Delta y H_y(\theta)\mathrm{e}^{i\omega_{ex}t}. \tag{7}$$

where $H_x=\cos(\theta)$ and $H_y=\sin(\theta)$ are the perturbed gap height variations in circumferential direction. The radial

displacements $\Delta x, \Delta y \ll 1$ are the small amplitudes of the excited motion around the equilibrium shaft position.The equilibrium gap height is given as follows:

$$H = H_{0r,g} + \varepsilon_x \cos(\theta) + \varepsilon_y \sin(\theta). \tag{8}$$

where $\varepsilon_x, \varepsilon_y$ are the static eccentricities in x- and y-direction. The pressure is also expressed as a perturbed property:

$$P_{per} = P_0 + \Delta x P_x(\theta, z) \mathrm{e}^{i\omega_{ex}t} + \Delta y P_y(\theta, z) \mathrm{e}^{i\omega_{ex}t}. \tag{9}$$

Inserting Eqs. (7) and (9) into Eq. (5) yields three equations, one for the static pressure P_0 and two for the perturbed, dynamic pressures P_x, P_y in the two coordinate directions x and y. The static pressure equation, or zeroth order equation is obtained by collecting all terms, which are not multiplied by Δx or Δy:

$$\begin{aligned} &\frac{\partial}{\partial\theta}\left(f_{1_0}\frac{\partial P_0^2}{\partial\theta} + f_{2_0}\frac{\partial P_0^2}{\partial Z} + 2c_s f_{4_0}\sin(\beta)P_0\right) + \\ &\frac{\partial}{\partial Z}\left(f_{2_0}\frac{\partial P_0^2}{\partial\theta} + f_{3_0}\frac{\partial P_0^2}{\partial Z} - 2c_s f_{4_0}\cos(\beta)P_0\right) = \\ &\qquad 2\Lambda\frac{\partial(P_0 f_{5_0})}{\partial\theta} \end{aligned} \tag{10}$$

where the subscript 0 marks the zeroth order properties. The dynamic pressure equations are obtained by collecting all first order terms ($\mathcal{O}(\Delta x), \mathcal{O}(\Delta y)$). Two equations are obtained by separating all terms, which are multiplied by Δx and all terms multiplied by Δy. The equation for P_x can be written as follows:

$$\begin{aligned} &\frac{\partial}{\partial\theta}\left[P_x f_{1_0}\frac{\partial P_0}{\partial\theta} + P_0 f_{1_x}\frac{\partial P_0}{\partial\theta} + P_0 f_{1_0}\frac{\partial P_x}{\partial\theta} + \right. \\ &\quad \left. P_x f_{2_0}\frac{\partial P_0}{\partial Z} + P_0 f_{2_x}\frac{\partial P_0}{\partial Z} + P_0 f_{2_0}\frac{\partial P_x}{\partial Z}\right] + \\ &\frac{\partial}{\partial Z}\left[P_x f_{2_0}\frac{\partial P_0}{\partial\theta} + P_0 f_{2_x}\frac{\partial P_0}{\partial\theta} + P_0 f_{2_0}\frac{\partial P_x}{\partial\theta} + \right. \\ &\quad \left. P_x f_{3_0}\frac{\partial P_0}{\partial Z} + P_0 f_{3_x}\frac{\partial P_0}{\partial Z} + P_0 f_{3_0}\frac{\partial P_x}{\partial Z}\right] + \\ &\qquad 2c_s\sin(\beta)\frac{\partial}{\partial\theta}\left(P_x f_{4_0} + P_0 f_{4_x}\right) - \\ &\qquad 2c_s\cos(\theta)\frac{\partial}{\partial Z}\left(P_x f_{4_0} + P_0 f_{4_x}\right) = \\ &\qquad 2i\gamma_{ex}\Lambda\left(P_0 f_{5_x} + P_x f_{5_0}\right) + \\ &\qquad \Lambda\frac{\partial\left(P_x f_{5_0} + P_0 f_{5_x}\right)}{\partial\theta} \end{aligned} \tag{11}$$

The dynamic pressure equation for P_y has exactly the same form, only the subscripts x are replaced by y. For solving Eqs. (10) and (11) the following Dirichlet boundary conditions are imposed at the bearing edges:

$$P_0 = 1, P_x = P_y = 0 \quad \text{on } \partial\Gamma. \tag{12}$$

On the whole fluid domain the pressure field has to fulfill the following periodicity requirement:

$$\begin{aligned} P_0(\theta, Z) &= P_0(\theta + 2\pi, Z), \\ P_{x,y}(\theta, Z) &= P_{x,y}(\theta + 2\pi, Z). \end{aligned} \tag{13}$$

The equations are discretized by a finite difference method (FDM) and the non-linearities are treated by the itertive Newton-Raphson method. The static bearing reaction forces are computed by integrating the unperturbed pressure field, which can be written in dimensionless form as follows:

$$F_x = -\int_{-L/D}^{L/D}\int_{0}^{2\pi} (P_0 - 1)\cos\theta d\theta dZ \tag{14}$$

$$F_y = -\int_{-L/D}^{L/D}\int_{0}^{2\pi} (P_0 - 1)\sin\theta d\theta dZ. \tag{15}$$

The bearing stiffness and damping values are obtained in analogy to the static forces by integrating the first order pressure fields P_x and P_y, obtaining the complex dynamic bearing force coefficients Z_{ij}. Based on the spectral analysis by Pan [17], Z_{ij} are computed for different whirl ratios $\gamma_{ex} = \omega_{ex}/\Omega$. In this work 41 whirl ratios are computed ranging from 0.01 to 2, including $\gamma_{ex} = 1$, which corresponds to the synchronous whirl condition where $\omega_{ex} = \Omega$. The 8 stiffness and damping values can then be extracted from Z_{ij} as follows:

$$\begin{bmatrix} Z_{xx} & Z_{xy} \\ Z_{yx} & Z_{yy} \end{bmatrix} = \begin{bmatrix} K_{xx} & K_{xy} \\ K_{yx} & K_{yy} \end{bmatrix} + i\gamma_{ex} \begin{bmatrix} C_{xx} & C_{xy} \\ C_{yx} & C_{yy} \end{bmatrix}. \tag{16}$$

The stiffness K_{ij} and damping C_{ij} values are finally used in the equations of motion for rotordynamic stability analysis. In order to characterize a HGJB, the static forces F_x and F_y and the eight stiffness and damping values K_{ij}, C_{ij} for each whirl ratio γ_{ex} need to be known. They are normally obtained by numerically solving one non-linear PDE for the static forces and two linear PDEs for the dynamic forces for 41 whirl ratios, yielding the computation of 83 PDEs in total. In

the following, a new approach is presented, which model the PDEs by ANNs. The ANNs need the numerical solutions at certain sample points in the parametere space for training, but once trained, the bearing force coefficients can be obtained directly. The main advantages of using ANNs are that the complexity of computing the HGJB properties is significantly reduced (only analytical functions need to be evaluated, instead of solving complex PDEs) and the computations can be performed fully vectorized, which results in significant speed up factors.

3. Methodology

Feed-forward neural network models. The investigation of artificial neural network (ANN) architectures is done separately for the static and dynamic response variables. The base architecture is a feed-forward neural network (FNN), which represents a non-linear function of its inputs and is composed by its neuron functions [2]. It consists of a fully-connected input layer, a few hidden layers and a fully connected output layer. A corresponding network is schematically shown in Fig. 2, which consists of 1 input layer with 6 inputs, two hidden layers with 7 and 4 neurons and 1 output layer with 1 output. A neuron is a non-linear mapping of several inputs to one output. Each neuron of a given layer is connected to each neuron of the preceding layer. A neuron is characterized by its activation function. On layer $n+1$

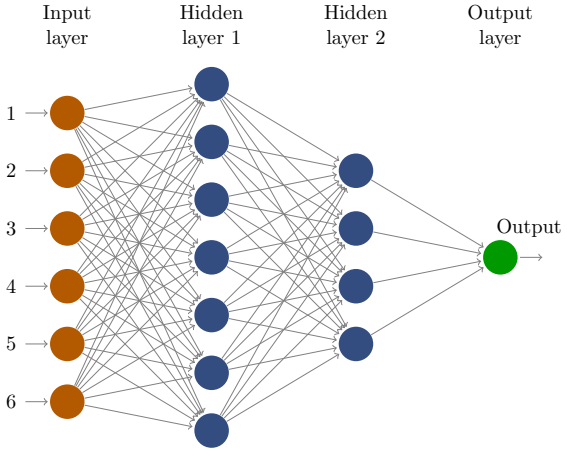

Figure 2: Schematic representation of feed-forward neural network with one input layer, two hidden layers and one output layer. The network accepts 6 inputs and returns one output. Hidden layer 1 has 7 neurons and hidden layer 2 has 4 neurons.

each neuron receives inputs x_i from all neuron outputs at layer n. These inputs are weighted and summed:

$$v = \sum_{i=1}^{m} w_i x_i + b \tag{17}$$

where m is the number of neuron input values, w_i are the weights for each input and b is an additional constant term, also named "bias". The value v is termed the potential of the neuron. The output of the neuron is computed by a

non-linear activation function g and the potential v. In this work, the hyperbolic tangent sigmoid activation function is selected, which is given as follows:

$$g(v) = \frac{2}{1 + e^{-2v}} - 1. \tag{18}$$

This activation function is used for all intermediate (hidden) layers. The final predicted value y_p is computed by the output neuron, which has a linear activation function:

$$y_p = cv, \tag{19}$$

where c is a constant and v is computed by Eq. (17).

In this work, six parameters are used as inputs and one parameter as output, i.e. a separate neural network is trained for each bearing output (static reaction forces and stiffness and damping force coefficients). In order to train the network, the weights w_i and the bias b have to be adjusted such that the output predicts the response variable. The model prediction error can be quantified by the mean-squared error (RMSE), which has to be minimized during training. The RMSE is defined as follows:

$$RMSE = \sqrt{\frac{1}{N} \sum_{i=1}^{N} \left(y_p^{(i)} - y^{(i)} \right)^2} \tag{20}$$

where N are the number of samples, y_p and y are the predicted and sample output values. The RMSE is not ideal for comparing different output parameters, since it is not a normalized property. Therefore the normalized root mean-squared error NRMSE is used, which is defined as:

$$NRMSE = \frac{\sqrt{\frac{1}{N} \sum_{i=1}^{n} (y_p^{(i)} - y^{(i)})^2}}{y_{max} - y_{min}}, \tag{21}$$

where y_{max} and y_{min} are the maximum and minimum values on the whole validation data set. The nominator of Eq. (21) represents the root mean squared error, which is normalized by the sample range.

The weights and bias of the FNN are updated by the Levenberg-Marquardt optimization algorithm by means of back-propagation, which is widely described in the literature (e.g. [2]). The Levenberg-Marquardt algorithm is an iterative numerical method, where the weights and the biases of the neural network are updated by the following expression:

$$\mathbf{x}_{k+1} = \mathbf{x}_k - \left[\mathbf{J}^T \mathbf{J} + \lambda_{lm} \mathbf{I} \right]^{-1} \mathbf{J}^T \mathbf{e}, \tag{22}$$

where λ_{lm} is a scalar, $\mathbf{x}$ is the vector containing all weights and biases, $\mathbf{e}$ is the network error vector (computed by the loss function) and $\mathbf{J}$ the corresponding Jacobian. Through iteration the weights and biases are updated, leading to a reduction in network errors. Backpropagation is one way of computing the Jacobian. The inputs and outputs of the neurons are computed by one forward-pass, the loss function is evaluated and its derivative computed. This value is then backpropagated to the first layer by computing the gradient of the weighted input of each layer. The two main advantages of this process are that there are no duplicated computations and that it computes the gradient directly to the output loss function and not to additional intermediate parameters.

FNN architecture for static force models. For identifying the static response models, different network widths and depths are investigated by varying the number of layers and corresponding neurons. The variation is performed on a dataset of 40k samples for a compressibility number interval of $\Lambda = [20, 25]$. All points with an eccentricity lower than $\varepsilon < 1 \times 10^{-4}$ are not considered, since the static reaction forces are close to zero and a regression model in this region is not meaningful. Each network is trained over a period of 100 epochs. Then the networks are characterized by a test sample dataset. The relative errors between sample ouput and prediction are computed. Based on these errors, the number of predictions laying outside the 2 % and 5 % relative error bounds are counted. The number of counts is used as a quality measure of the model prediction accuracy.

The net variation for the response variable F_x is shown in Fig. 3a with the corresponding accuracy of fit in Fig. 3b. As expected, the accuracy increases for two layer architectures and an increased number of neurons. If the number of neurons on the first layer is larger than 30 and on the second layer larger than 20, the accuracy does not significantly increase with further increasing the layer width. The various networks are screened by applying the desired error threshold of $p_{0.02} < 0.02$, which means that up to 2 % of the dataset points are predicted by the model with an error larger than 2 %. Among the networks, fulfilling this requirement, the one with the lowest number of total neurons is chosen, in order to reduce the training time later on. The optimum model for F_x is identified in Fig. 4. It has two layers with 30 and 21 neurons. In analogy the model found for response variable F_y has two layers with 36 and 21 neurons.

FNN architecture for dynamic force models. The net structures for the dynamic force coefficients are developed by assessing the stiffness and damping values K_{ij}, C_{ij} with the largest variations along the parameter variation, which is the cross-coupled damping C_{xy}. The nets are trained and tested in the compressibility number range $\Lambda = [35, 40]$ with 34k samples. The two layer net structure variations are shown in Fig. 5a. The corresponding accuracy of fit is shown in Figs. 5b and 5c. $p_{0.02} < 0.02$ is chosen as a net selection criterion. Under the remaining network architectures, fulfilling this criterion, the one with the lowest total number of neurons is chosen. The optimum model is identified in Fig. 6 and has 36 neurons on the first layer and 13 on the second layer. This particular net architecture was used for fitting the stiffness and damping values K_{ij}, C_{ij} at each whirl ratio and compressibility number interval.

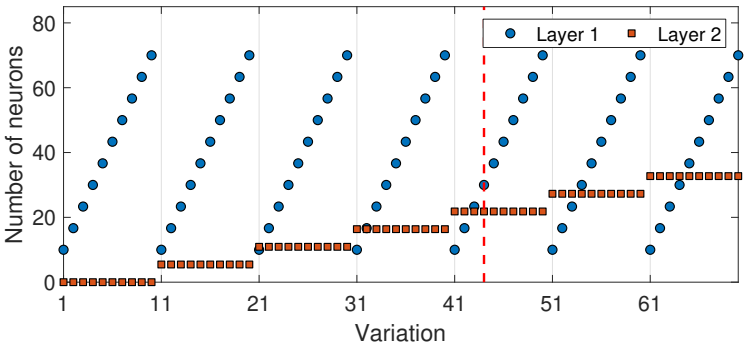

(a) Number of neurons of layer 1 and layer 2 of a FNN.

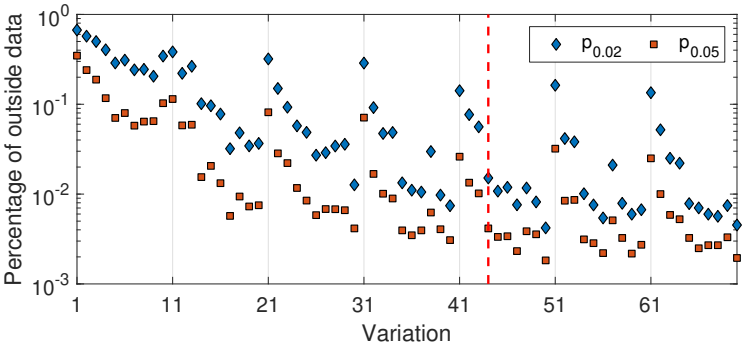

(b) Percentage of data outside the 2 % and 5 % region.

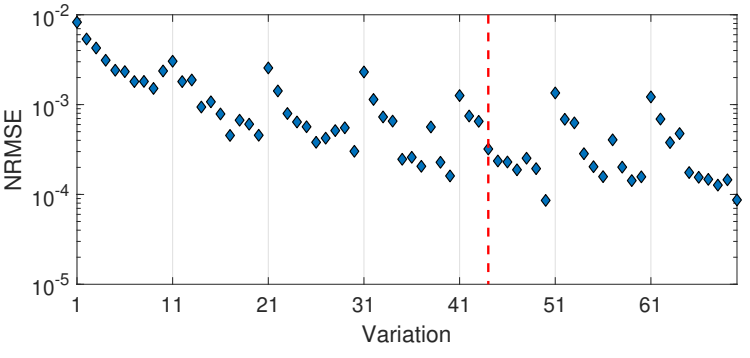

(c) NRMSE below 5×10^{-4} for train, test and validation data set.

Figure 3: Neural network variation for response variable F_x. Dashed red line: selected network architecture. The variation number corresponds to a given combination of the number of neurons on the first and the second layer.

4. Meta-model performance

Static force models. For modeling the static forces F_x and F_y, the neural networks presented above are used for fitting sample data. The compressibility number range $\Lambda = [0.1, 40]$ is subdivided into 8 intervals. The reason for the subdivision into compressibility number ranges is the reduction of degrees of freedom the model has to handle, which allows for the usage of simpler and faster models. The first interval has the limits $[0.1, 5]$, the others are all starting at multiples of 5 with length $\Delta\Lambda_{12} = 5$. This value has been selected by testing different interval length. For each interval a model is trained. The training data consists of a total of 310k samples, from which 82 % belong to a full

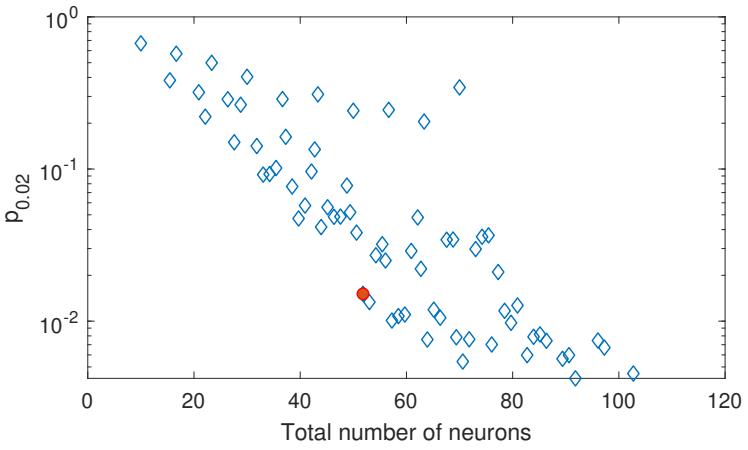

Figure 4: Neural network selection by two objective variables, the percentage of data outside 2 % error band (1) versus the total number of neurons of two layers (2). Filled circle: performance of selected net architecture with $p_{0.02} < 2\,\%$ and minimum number of total neurons for the static force prediction.

factorial distribution. The number of training data points has been selected based on reasonable computation times for creating the test data set (within weeks) and avoiding sub-sampling of the solution parameter space. The models are tested by 120k randomly distributed data points per compressibility number interval, which have not been used for training. The fit of accuracy is quantified by the NRMSE for each compressibility number interval and summarized in Fig. 7. It can be seen that the regression models accuracy increases towards larger compressibility numbers. The largest difference is observed at the compressibility number interval $[0.1, 5]$ with a NRMSE of 7×10^{-4}.

The regression model is compared with solving the NGT lubrication equation directly. The computation time of the NGT equation is dependent on solver parameters, the bearing geometry and its operational condition. If these are kept constant, the computation time for a certain variation is a linear function of the number of computations. Since the meta-model is fully vectorized, the computation time is not a linear function of the number of computations. This is shown in Fig. 8, where the total time for a given number of computations is compared between solving the NGT directly and using the derived meta-model. It can be seen, that with increasing the number of computations, the speed-up factor increases until leveling off at $> 10^5$ for $> 10^5$ computations. It can be concluded, that the meta-model is significantly more efficient in handling large datasets, than it is for low number of computations, while achieving very low deviation to the original and more complex NGT model.

Dynamic force models. The stiffness and damping values are trained individually for each whirl ratio. The 8 dynamic forces K_{ij}, C_{ij} and 41 whirl ratios [0.01-2] yield 328 models per compressibility number interval. 41 discrete whirl ratios are selected in order to resolve the strong non-linear variations of dynamic force coefficients (see Fig. 12). The whirl ratio could be regarded as an additional input parameter to the models, reducing the number of models to 8. However, the training data set would be larger by factor 41 and the model complexity would increase in order to handle

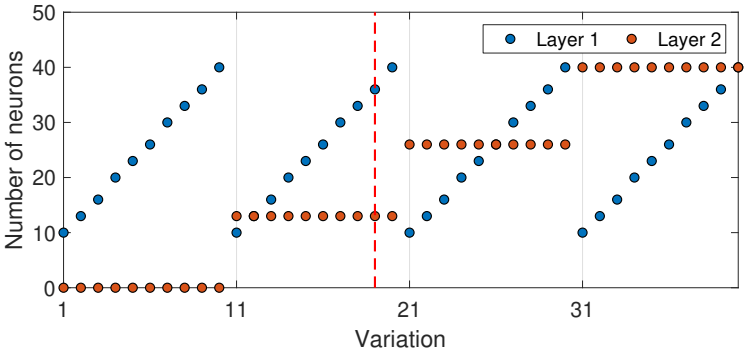

(a) Number of neurons of layer 1 and layer 2 of a feed-forward neural network.

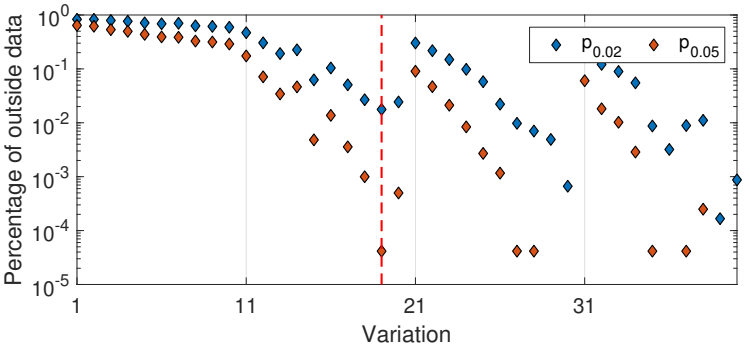

(b) Percentage of data outside the 2 % and 5 % region.

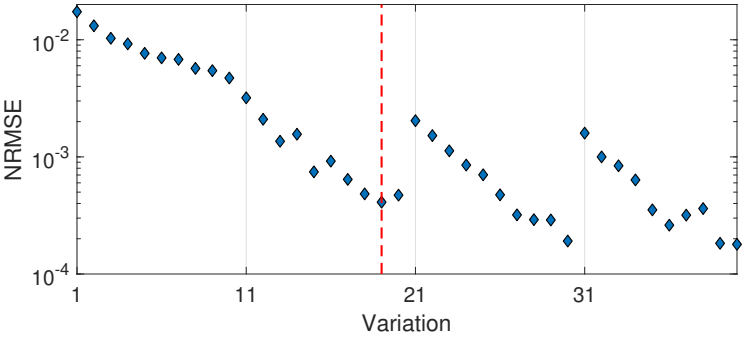

(c) Normalized root mean squared error below 5×10^{-4} for train, test and validation data set.

Figure 5: Neural network variation for response variable C_{xy}.. Dashed red line: selected network architecture.The variation number corresponds to a given combination of the number of neurons on the first and the second layer.

the additional degree of freedom. Based on these facts, a dynamic force coefficient model per whirl ratio and compressibility interval was trained. The compressibility number intervals are [1-2, 2-5, 5-10, 10-20, 20-30, 30-40], which have been selected by testing different subdivisions and comparing training time and model prediction accuracy. The smaller intervals for lower compressibility numbers accounts for the stronger variation of dynamic bearing properties with compressibility number in this region. The models are trained by 2.3×10^6 samples, where 57 % are full factorial and the remainder randomly distributed data points. The models are trained until the RMSE showed convergence, i.e. the change of RMSE over epochs approaches 0. The RMSE convergence of the cross-coupled damping C_{xy}, at the

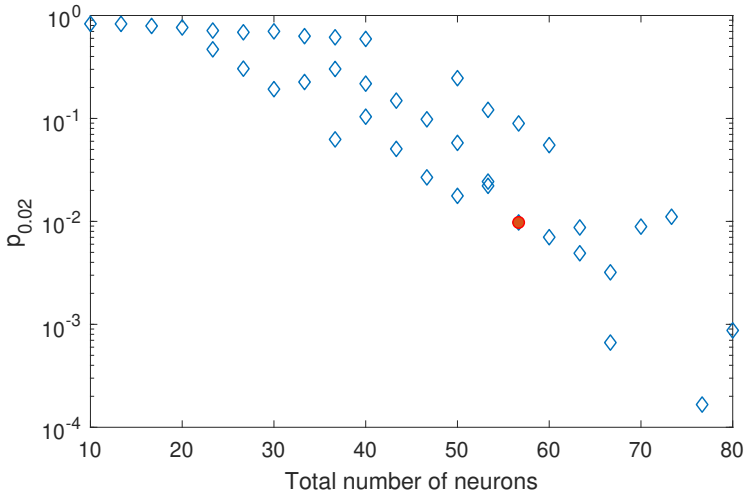

Figure 6: Neural network selection by two objective variables, the percentage of data outside 2 % error band (1) versus the total number of neurons of two layers (2). Filled circle: performance of selected net architecture with $p_{0.02} < 2\,\%$ and minimum number of total neurons for the cross-coupled stiffness and damping force coefficients.

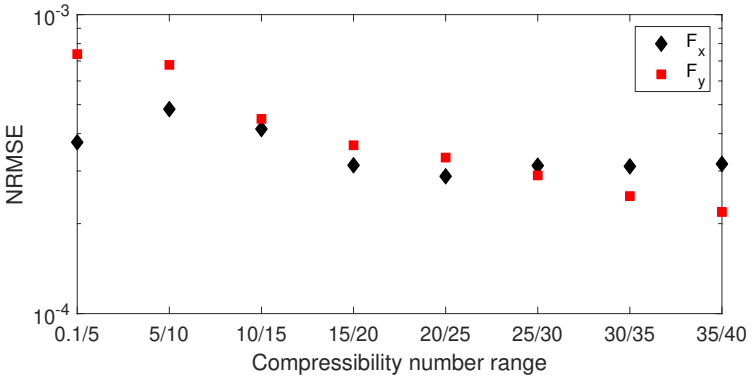

Figure 7: FNN performance evaluation for response variables F_x and F_y. Normalized root mean squared error below 7×10^{-4} for 120k randomly distributed data points per compressibility number interval.

whirl ratio $\gamma_{ex} = 1$, for the compressibility number interval $\Lambda = [1, 2]$, is shown in Fig. 9. It can be seen, that after 50 epochs the change of RMSE is not significant and a further training yields only a small increase in accuracy. The models are validated by 55k randomly distributed data points (geometry and eccentricity) in the compressibility range of $\Lambda = [1, 40]$, which have not been used for training. The accuracy of the models is quantified by the NRMSE. The results are shown in Figs. 10 and 11. In Fig. 10 the maximum NRMSE of all whirl ratios in a given compressibility number range, is plotted for all dynamic bearing coefficients. It can be seen that all NRMSE are below 0.01, which has been set as the training target. In Fig. 11 the maximum NRMSE of the whole validation data set is shown at different whirl ratios. It can be seen that the models perform equally well at different whirl ratios.

A comparison of predicted and excact solution for the impedances is shown in Fig. 12. The data point was not used in the training set. It can be seen that the model shows very good agreement with the NGT computed data.

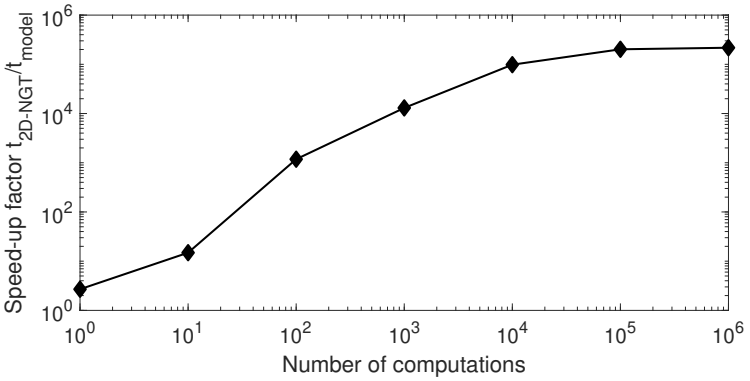

Figure 8: Computation time comparison of regression model and numerically solving the NGT equation.

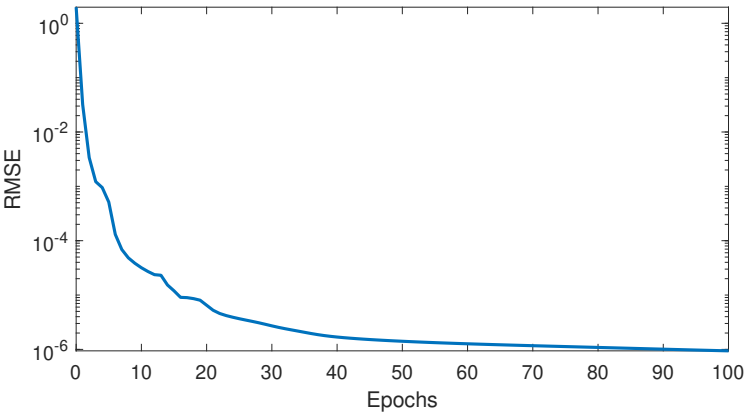

Figure 9: RMSE convergence of C_{xy} at whirl ratio $\gamma_{ex} = 1$, in the compressibility number interval $\Lambda = [1, 2]$.

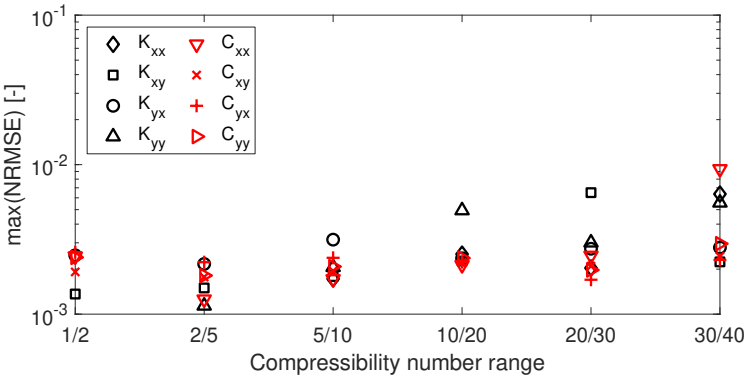

Figure 10: Evaluation of stiffness and damping meta models. Maximum NRMSE for different compressibility number intervals.

By using the meta-models a significant speed-up can be achieved compared to solving the NGT numerically (Fig. 13). A similar trend as for the meta-models for the static forces can be observed. For one single computation, the meta-model is slower than using the NGT solver, which can be attributed to the neural network initialization. However,

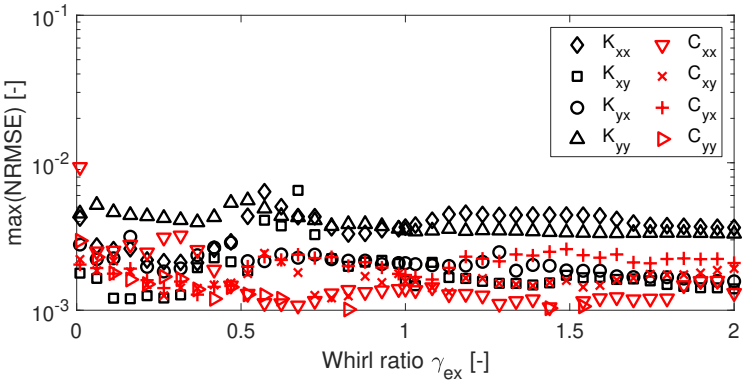

Figure 11: Evaluation of stiffness and damping meta models. Maximum NRMSE at different whirl ratios and all compressibility numbers.

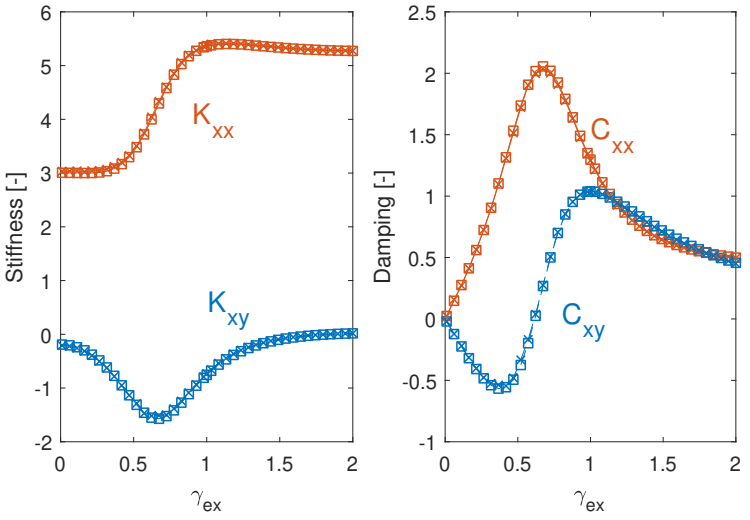

Figure 12: Comparison of model with numerical data. Stiffness and damping values of bearing operating at $\Lambda = 23$. Crosses: model, squares: numerical data.

already at 10 computations, the meta-models yield a speed-up factor of approximately 10. At 10^4 computations the speed-up factor levels off at around 3000. This speed-up reduces the computation time of a typical bearing optimization that takes several days down to minutes, which allows for large parameter variations in a reasonable amount of time without incurring significant deviation to the NGT model. In addition, eccentric shaft positions can be computed at arbitrary values. The meta-models are not limited to discrete values and multi-dimensional interpolations are possible, which is shown in the following section by means of a multi-objective rotordynamic system optimization.

5. Case study

The strength of the developed models is presented by means of a real case rotordyamic system optimization, encountered in the development phase of small scale oil-free turbomachines. In order to validate the ANN models, the

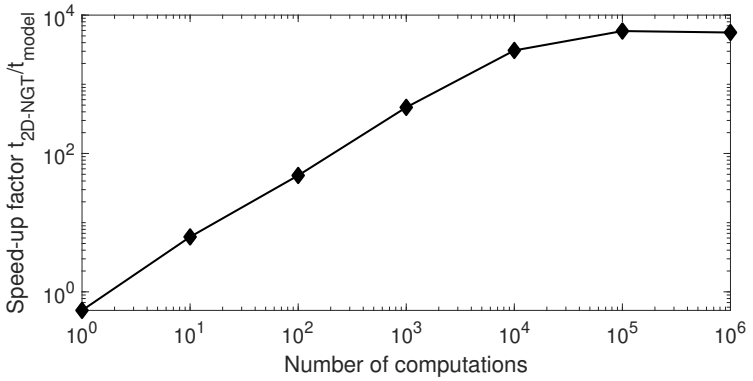

Figure 13: Computation time comparison of regression model and numerically solving the NGT equation for stiffness and damping values for 41 whirl ratios.

optimum solution, obtained with the ANN, is compared with the solution obtained by solving the PDEs directly.

Rotordynamic model. The design of small-scale turbomachinery requires stability analysis of the complete rotordynamic system, considering the bearing non-linear stiffness and damping values. The system may be optimized for maximum load capacity and stability. The load capacity can be directly quantified by the radial force in x-direction (see Eq. (14)). The rotordynamic stability is computed by a natural frequency analysis of the bearing-shaft system. The pure radial motion of a shaft, modeled as a point-mass, can be described by the following system of equations:

$$\mathbf{M}\ddot{x} + \mathbf{C}\dot{x} + \mathbf{K}x = 0 \tag{23}$$

where $\mathbf{M}$ is the mass matrix:

$$\mathbf{M} = \begin{bmatrix} m & 0 \\ 0 & m \end{bmatrix}, \tag{24}$$

$\mathbf{C}$ the damping matrix:

$$\mathbf{C} = \begin{bmatrix} C_{xx} & C_{xy} \\ C_{yx} & C_{yy} \end{bmatrix}, \tag{25}$$

and $\mathbf{K}$ the stiffness matrix:

$$\mathbf{K} = \begin{bmatrix} K_{xx} & K_{xy} \\ K_{yx} & K_{yy} \end{bmatrix}. \tag{26}$$

The following non-dimensional properties can be introduced:

$$\bar{X} = \frac{x}{R} \tag{27}$$

as the shaft displacement with R as the bearing radius,

$$\tau = \gamma_{ex}\Omega t, \tag{28}$$

as the dimensionless time,

$$\bar{m} = \frac{p_a h_0^5}{36\mu^2 R^6}\gamma_{ex}^2\Lambda^2 m = m_d\gamma_{ex}^2\Lambda^2 \tag{29}$$

as the dimensionless mass, with p_a the ambient pressure, h_0 the bearing clearance, μ the dynamic fluid viscosity, Λ the compressibility number and m the shaft mass. The non-dimensional damping and stiffness coefficients can be written as follows:

$$\bar{C}_{ij} = \frac{h_0\gamma_{ex}\Omega}{p_a R^2}C_{ij} \tag{30}$$

$$\bar{K}_{ij} = \frac{h_0}{p_a R^2}K_{ij}. \tag{31}$$

With these definitions, Eq. (23) can be written as follows:

$$\bar{\mathbf{M}}\ddot{\bar{X}} + \bar{\mathbf{C}}\dot{\bar{X}} + \bar{\mathbf{K}}\bar{X} = 0. \tag{32}$$

By setting $\bar{X} = \bar{X}_s e^{\frac{\lambda\tau}{\gamma_{ex}\Omega}} = \bar{X}_s e^{\bar{\lambda}\tau}$ into Eq. (32), it follows the quadratic eigenvalue problem:

$$\left(\bar{\mathbf{M}}\bar{\lambda}^2 + \bar{\mathbf{C}}\bar{\lambda} + \bar{\mathbf{K}}\right)\bar{X}_s = 0 \tag{33}$$

which yields four eigenvalues, each coming as a complex conjugated pair of the following form:

$$\bar{\lambda}_{1,2} = -\bar{\delta} \pm i\sqrt{\bar{\omega}^2 - \bar{\delta}^2}. \tag{34}$$

From these, the logarithmic decrement can be computed which is > 0 if the system is stable and < 0 if the system is unstable. It can be represented by the following expression:

$$\Gamma = \frac{2\pi\bar{\delta}}{\sqrt{\bar{\omega}^2 - \bar{\delta}^2}}. \tag{35}$$

Two logarithmic decrements are computed for the two complex conjugated pairs of eigenvalues. One corresponds to a forward and one to a backward whirling shaft motion. Since the bearing impedance, and therefore the stiffness and damping matrices, $\bar{\mathbf{K}}$ and $\bar{\mathbf{C}}$, are whirl ratio dependent, Γ has to be computed for each whirl ratio γ_{ex}. The relevant logarithmic decrements (forward and backward whirling) at a given compressibility number are then obtained by finding γ_{ex}, where $\Im(\bar{\lambda})_{1,2} = 1$. The minimum logarithmic decrement of the backward and forward mode is considered for stability analysis and ideally, is maximized. This results in a logarithmic decrement for each bearing geometry, at each eccentricity and compressibility number. The system has to be stable over the whole compressibility number range and different eccentricities.

Optimization problem. The geometrical parameters of a HGJB are optimized for a given rotordynamic system, where the non-dimensional lumped mass of the selected test shaft is given by $m_d = 0.1578$. The HGJB geometry has to be found in order to maximize stability and load capacity. The HGJB parameters α, β, H_{gr} and L/D are optimized, assuming that each bearing has to support half the shaft mass $0.5m_d = 0.0789$. The bearing is assumed to work in the compressibility number interval $\Lambda = [0, 30]$, which is typical in real case applications (see Guenat and Schiffmann [8]). Since the lubrication equation and the rotordynamic analysis is performed fully non-dimensional, the only relevant parameter for describing the operational condition is the compressibility number. It contains any combination of viscosity and pressure values. Therefore it considers also viscosity variations with temperature changes.
The stability is analyzed at eccentricities $\varepsilon = 0$ and 0.5 and the load capacity is evaluated at $\varepsilon = 0.5$. The compressibility number range is subdivided into 30 points, thus leading to 60 computations per geometry. A multi-objective genetic optimization is performed with 2k geometries per population. The fitness function first computes the bearing stiffness and damping values K_{ij}, C_{ij}, by using the derived ANNs, then solves Eq. (33) for the system natural frequencies. The scores s_1 and s_2 of the fitness function are finally computed by:

$$\begin{aligned} s_1 &= -\min(\Gamma_{f,b}) \\ s_2 &= -\max(F_x). \end{aligned} \tag{36}$$

The minus signs are used since the optimization algorithm minimizes the scores and we are interested in maximum $\Gamma_{f,b}$ and F_x values. The total number of individual computations per population is 120k. On an Intel(R) Core(TM) i7-8550U CPU @ 1.80GHz processor, the computation time for one population (120k) is 147 s.

Results. The Pareto curve of the rotordynamic system optimization at generation 10 is shown in Fig. 14 and suggests a clear trade-off between stability and load capacity. The corresponding design variables along the Pareto front are represented in Fig. 15, which suggest that increased load capacity is achieved by reducing the effect of the grooves (reduced groove width and depth) and by increasing the L/D ratio.

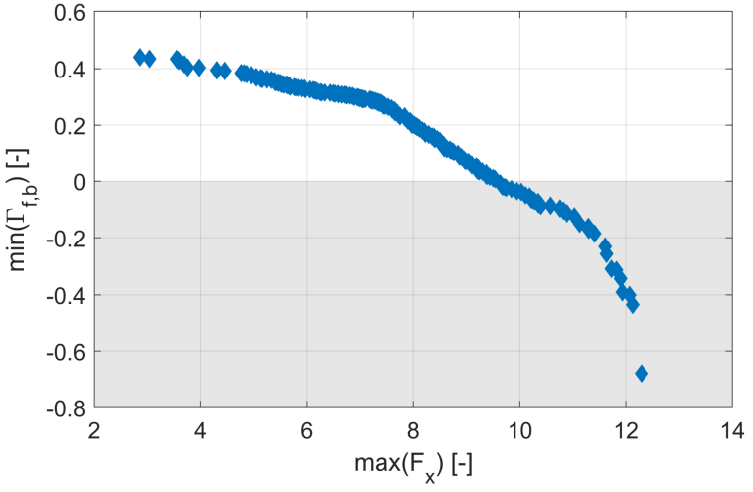

Figure 14: The Pareto curve for the optimized rotordynamic system in terms of minimum stability (at $\varepsilon = 0$ and 0.5) and maximum load capacity (for $\varepsilon = 0.5$) at generation 10. Gray region corresponds to unstable region.

A minimum logarithmic decrement of < 0 (gray region in Fig. 14) represents systems of unstable behavior and are not interesting in practice. The remaining geometries are chosen based on a trade-off between stability safety margin and achievable load capacity at eccentricity $\varepsilon = 0.5$.

Model performance and accuracy. The meta-model approach provides significant computation time improvements, compared to the direct finite difference method (FDM). For 10 generation a total number of 1.32 million single computations have to be performed. By using the meta-models, the computation of 10 generations, including the computation of the rotordynamic stability, takes a total time of 27 min. The same amount of computations, using the FDM with 4 parallel processes, would take (one single computation takes 1.5 s) 5.7 days, which corresponds to a factor ≈ 300, compared to the meta-model based optimization.

In order to assess the accuracy of the ANNs compared to the classical FDM approach in predicting the rotordynamic performance, the system natural frequencies and the corresponding logarithmic decrements are computed for all compressibility numbers and eccentricities with the ANN and the FDM approach (exact) for a solution selected on the computed Pareto curve. The selected design yields a logarithmic decrement of $\min(\Gamma_{f,b}) = 0.2018$ and a load capacity $\max(F_x) = 8.0138$. The corresponding optimization parameters are $\alpha = 0.486$, $\beta = 46.9°$, $H_{gr} = 1.819$ and $L/D = 1.783$. The comparison is summarized in Table 3. The relative error between FDM and meta-model approach for the minimum stability is 1.1 % and the error for predicting the static radial bearing reaction force is <0.1 %.

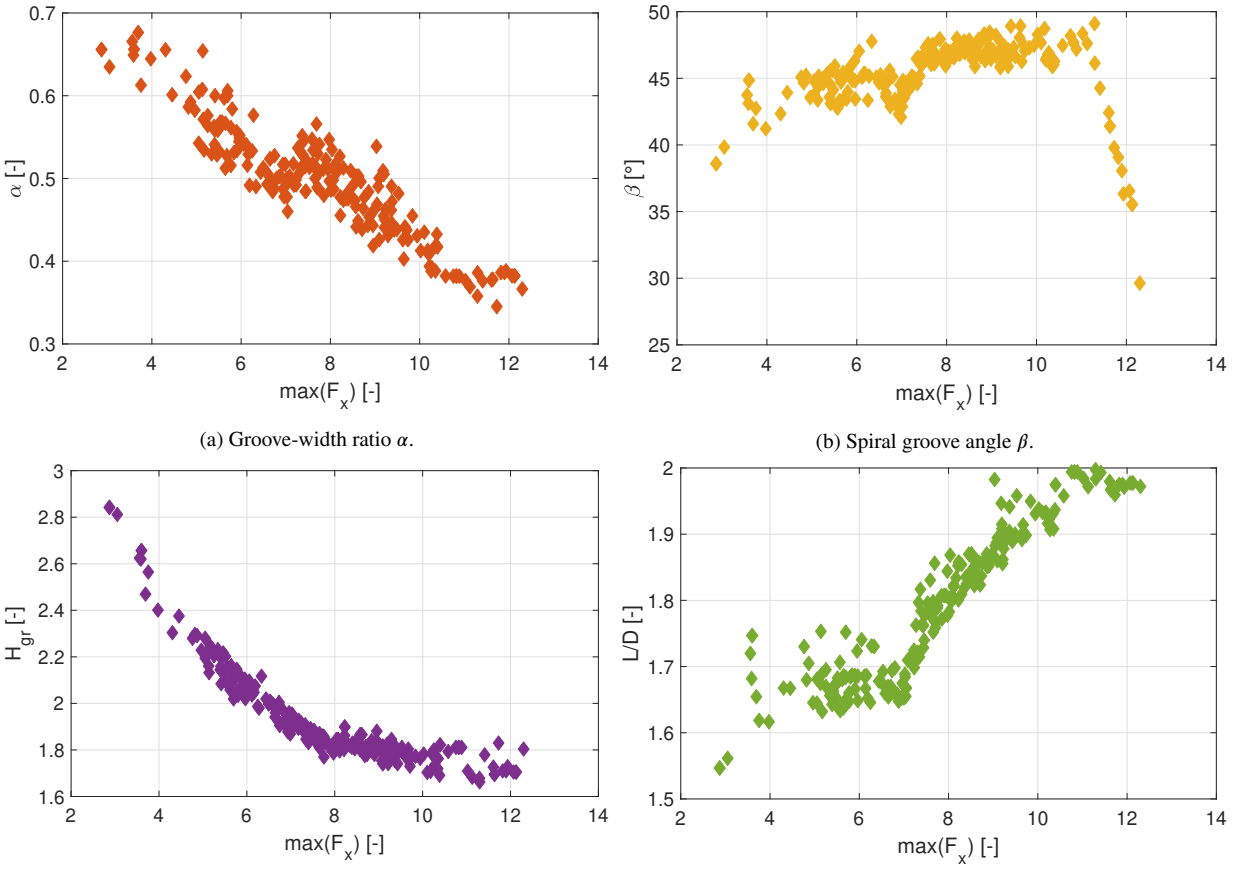

(a) Groove-width ratio α.

(b) Spiral groove angle β.

(c) Groove depth ratio H_{gr}.

(d) Length to diameter ratio L/D.

Figure 15: Pareto optimum for different HGJB geometrical parameters as a function of maximum radial force F_x, at generation 10.

Table 3
Result comparison of optimized geometry between FDM and meta-model approach.

Score value	FDM	Meta-model	Rel. error
$\min(\Gamma_{f,b})$	0.204	0.2018	0.011
$\max(F_x)$	8.0193	8.0138	0.0007

6. Summary and Conclusion

Data-driven meta-modeling of the static and dynamic analysis of HGJBs are presented in view of speeding up bearing computation time and enhancing bearing analysis possibilities.

Feed-forward neural networks (FNN) are used, offering many degrees of freedom and the possibility of fitting highly non-linear data sets. The models are tested and derived for predicting the static and dynamic HGJB behavior in different compressibility number intervals and eccentric shaft positions.

It can be concluded, that with two layer neural network architectures, a meta-model for the static reaction forces F_x and F_y can be trained with a NRMSE $<7 \times 10^{-4}$. For the dynamic force coefficients K_{ij} and C_{ij} a NRMSE $<1 \times 10^{-2}$

is achieved.

The ANNs offer significant computational speed-up, in particular towards a high number of computations. At 10^4 computations the speed-up factor levels-off at $> 10^5$ for the static force models and $> 10^3$ for the dynamic force models. This means a significant reduction in bearing computation time, allowing for large (in the range of millions) parameter variations in minutes.

The ANNs are trained in parameter intervals, which gives the possibilities for multi-dimensional interpolation, avoiding discrete point limitations. The models can predict the bearing reaction forces at arbitrary eccentric positions, which makes them ideally suited for being used in a rotordynamic context. The subdivision into compressibility number intervals leads to a reduction of parameter space size, which makes it possible to use simple and fast FNN architectures. Furthermore, it allows for easily expanding the models towards larger compressibility numbers.

The ANNs can be smoothly integrated in a rotordynamic context, allowing for time-efficient, optimizations. A relative difference of <1.1 % has been observed between the ANN based model and the classical FDM based approach for the target optimization parameter values. The meta-models lead to a speed-up factor for rotordynamic computations of ≈ 300, which reduces the computation time from several days to minutes.

Nomenclature

Acronyms

$\bar{C}_{ij}$	Non-dimensional damping, $p_a R^2/(h_0 \gamma_{ex} \Omega) C$
$\bar{K}_{ij}$	Non-dimensional stiffness, $p_a R^2/h_0 K$
$\bar{m}$	Non-dimensional mass, $m_d \gamma_{ex}^2 \Lambda^2$
$\mathbf{e}$	Network error vector
$\mathbf{J}$	Jacobian of weigths and biases
$\mathbf{x}$	Vector containing all weights and biases
b	bias
c_s	NGT coefficient
C_{ij}	Damping coefficients (Ns/m)
D	Diameter (m)
f	NGT coefficient
g	Activation function
H	Non-dimensional gap height
h	Gap height μm
i	Imaginary number
K_{ij}	Stiffness coefficients (N/m)
L	Bearing length (m)
m	Mass (kg)
m_d	Non-dimensional mass, $p_a h_0^5/(36\mu^2 R^6) m$
N	Natural number
n	Layer number
P	Non-dimensional pressure
p_a	Ambient pressure (Pa)
q	Solution variable
R	Radius (m)
v	Potential of neuron
w	Width m
w_i	Neuron weights
x	Neuron input
y	Response variable

Z Non-dimensional axial coordinate, $Z = z/R$

z Axial coordinate (m)

Z_{ij} Non-dimensional impedance coefficients

Greek Symbols

α Dimensionless groove width

$\bar{\delta}$ Damping value

$\bar{\omega}$ Eigenfrequency

β Groove angle (°)

γ Dimensionless groove length

γ_{ex} Whirl ratio, ω_{ex}/Ω

$\Gamma_{f,b}$ Logarithmic decrement

Λ Compressibility number, $6\mu\Omega/p_a(R/h)^2$

λ Eigenvalue

λ_{lm} Scalar for Levenber-Marquardt algorithm

μ Dynamic viscosity (Pa · s)

Ω Rotational speed (rad/s)

ω_{ex} Excitation frequency (rad/s)

ϕ Attitude angle (°)

τ Non-dimensional time, $\omega_{ex}t$

θ Circumferential coordinate (rad)

ε Dimensionless eccentricity, e/h_0

e Eccentricity (µm)

Subscripts

0 Concentric position

$\bar{X}$ Non-dimensional x-direction coordinate, x/R

θ Circumferential direction (rad)

a Ambient

g Groove

gr Ratio groove to ridge

l Land region

r Ridge

s Solution variable

x x-direction in shaft cross-section plane (m)

y y-direction in shaft cross-section plane (m)

z Axial direction (m)

ANN Artificial neural network

FGA Finite Groove Approach

FNN Feedforward neural network

HGJB Herringbone groove journal bearing

NGT Narrow-groove theory

NRMSE Normalized root mean squared error

PDE Partial differential equation

RMSE Mean squared error

References

[1] Bonneau, D., Absi, J., 1994. Analysis of Aerodynamic Journal Bearings With Small Number of Herringbone Grooves by Finite Element Method. Journal of Tribology 116, 698–704. doi:10.1115/1.2927320.

[2] Dreyfus, G., 2004. Neural Networks. 2nd ed., Springer International Publishing, Berlin. doi:10.1007/978-3-030-11869-3_2.

[3] Elrod, H.G., McCabe, J.T., Chu, T.Y., 1967. Determination of Gas-Bearing Stability by Response to a Step-Jump. Journal of Lubrication Technology 89, 493. doi:10.1115/1.3617042.

[4] Fleming, D.P., Hamrock, B.J., 1974. Optimization of self-acting herringbone journal bearing for maximum stability. NASA Technical Memorandum .

[5] Franssen, R., Potze, W., de Jong, P., Fey, R., Nijmeijer, H., 2017. Large amplitude dynamic behavior of thrust air bearings: Modeling and experiments. Tribology International 109, 460–466. URL: https://www.sciencedirect.com/science/article/pii/S0301679X16304960, doi:10.1016/J.TRIBOINT.2016.12.024.

[6] Gu, L., Guenat, E., Schiffmann, J., 2019. a Review of Grooved Dynamic Gas Bearings. Applied Mechanics Reviews doi:10.1115/1.4044191.

[7] Guenat, E., Schiffmann, J., 2018. Effects of humid air on aerodynamic journal bearings. Tribology International 127, 333–340. doi:10.1016/j.triboint.2018.06.002.

[8] Guenat, E., Schiffmann, J., 2019. Multi-Objective Optimization of Grooved Gas Journal Bearings for Robustness in Manufacturing Tolerances. Tribology Transactions 62, 1041–1050. doi:10.1080/10402004.2019.1642547.

[9] Hassini, M.A., Arghir, M., 2012. A Simplified Nonlinear Transient Analysis Method for Gas Bearings. Journal of Tribology 134, 011704. doi:10.1115/1.4005772.

[10] Hassini, M.A., Arghir, M., 2013. A New Approach for the Stability Analysis of Rotors Supported by Gas Bearings. Journal of Engineering for Gas Turbines and Power 136, 022504. doi:10.1115/1.4025483.

[11] Hassini, M.A., Arghir, M., 2015. A Simplified and Consistent Nonlinear Transient Analysis Method for Gas Bearing: Extension to Flexible Rotors. Journal of Engineering for Gas Turbines and Power 137, 092502. doi:10.1115/1.4029709.

[12] Hirs, G.G., 1965. The Load Capacity and Stability Characteristics of Hydrodynamic Grooved Journal Bearings. ASLE Transactions 8, 296–305. doi:10.1080/05698196508972102.

[13] Iseli, E., Guenat, E., Tresch, R., Schiffmann, J., 2020. Analysis of spiral-grooved gas journal bearings by the narrow-groove theory and the finite element method at large eccentricities. Journal of Tribology 142. doi:10.1115/1.4045636.

[14] Malanoski, S.B., Pan, C.H.T., 1965. The Static and Dynamic Characteristics of the Spiral-Grooved Thrust Bearing. Journal of Basic Engineering 87, 547–555. doi:10.1115/1.3650603.

[15] Miller, B., Green, I., 1997. On the Stability of Gas Lubricated Triboelements Using the Step Jump Method. Journal of Tribology 119, 193. doi:10.1115/1.2832458.

[16] Miller, B., Green, I., 1998. Constitutive Equations and the Correspondence Principle for the Dynamics of Gas Lubricated Triboelements. Journal of Tribology 120, 345. doi:10.1115/1.2834433.

[17] Pan, C.H.T., 1964. Spectral analysis of gas bearing systems for stability studies. Technical Report. Mechanical Technology Inc Latham NY.

[18] Rosset, K., Mounier, V., Guenat, E., Schiffmann, J., 2018. Multi-objective optimization of turbo-ORC systems for waste heat recovery on passenger car engines. Energy 159, 751–765. doi:10.1016/j.energy.2018.06.193.

[19] San Andrés, L., Jeung, S.H., 2015. Orbit Model Force Coefficients for Fluid Film Bearings : A Step Beyond Linearization. ASME Turbo Expo 2015: Turbine Technical Conference and Exposition 7A, V07AT31A020. doi:10.1115/GT2015.

[20] Schiffmann, J., 2015. Integrated Design and Multi-objective Optimization of a Single Stage Heat-Pump Turbocompressor. Journal of Turbomachinery 137, 071002. doi:10.1115/1.4029123.

[21] Vohr, J., Pan, C., 1964. On the spiral grooved, self-acting, gas bearing. Mechanical technology Inc Latham NY No. 63TR52.
[22] Vohr, J.H., Chow, C.Y., 1965. Characteristics of herringbone-grooved, gas-lubricated journal bearings. Journal of Basic Engineering 87, 568. doi:10.1115/1.3650607.
[23] Whipple, R., 1958. The inclined groove bearing. Technical Report. United Kingdom Atomic Energy Authority. Research Group. Atomic Energy Research Establishment. Harwell, Berks, England.
[24] Zhao, D., Blunier, B., Gao, F., Dou, M., Miraoui, A., 2014. Control of an ultrahigh-speed centrifugal compressor for the air management of fuel cell systems. IEEE Transactions on Industry Applications 50, 2225–2234. doi:10.1109/TIA.2013.2282838.